Computing Thickness of Irregularly-Shaped Thin Walls Using a Locally Semi-Implicit Scheme with Extrapolation to Solve the Laplace Equation: Application to the Right Ventricle[★]

Susana **Merino-Caviedes**[a,*], Marcos **Martín-Fernández**[a], María Teresa **Pérez Rodríguez**[b], Miguel Ángel **Martín-Fernández**[a], David **Filgueiras-Rama**[c,1], Federico **Simmross-Wattenberg**[a] and Carlos **Alberola-López**[a]

[a]*Laboratorio de Procesado de Imagen, ETSI Telecomunicación, Universidad de Valladolid, Valladolid, Spain*
[b]*Escuela de Ingenierías Industriales, Universidad de Valladolid, Valladolid, Spain*
[c]*Centro Nacional de Investigaciones Cardiovasculares (CNIC), Novel Arrhythmogenic Mechanisms Program, Madrid, Spain*

ARTICLE INFO

ABSTRACT

Cardiac Magnetic Resonance (CMR) Imaging is currently considered the gold standard imaging modality in cardiology. However, it is accompanied by a tradeoff between spatial resolution and acquisition time. Providing accurate measures of thin walls relative to the image resolution may prove challenging. One such anatomical structure is the cardiac right ventricle. Methods for measuring thickness of wall-like anatomical structures often rely on the Laplace equation to provide point-to-point correspondences between both boundaries. This work presents *limex*, a novel method to solve the Laplace equation using ghost nodes and providing extrapolated values, which is tested on three different datasets: a mathematical phantom, a set of biventricular segmentations from CMR images of ten pigs and the database used at the RV Segmentation Challenge held at MICCAI'12. Thickness measurements using the proposed methodology are more accurate than state-of-the-art methods, especially with the coarsest image resolutions, yielding mean L_1 norms of the error between 43.28% and 86.52% lower than the second-best methods on the different test datasets. It is also computationally affordable. *Limex* has outperformed other state-of-the-art methods in classifying RV myocardial segments by their thickness.

1. Introduction

Magnetic Resonance (MR) is a medical image modality that provides very good contrast between soft tissues; this technique is able to acquire images using arbitrary plane orientations and has many different contrast possibilities that suit a broad range of clinical purposes. Specifically, cardiac MR (CMR) is currently considered the gold standard for evaluating myocardial function, volumes, and scarring [31]. This imaging modality, however, is accompanied by a tradeoff between spatial resolution and acquisition time, since pixel size is inversely proportional to the extension of the acquired k-space. For Cartesian sampling schemes, which are customary in CMR clinical studies, high resolution quality images take long acquisition times [21]. Consequently, and very specially for the cases in which images are acquired in apnea, image resolution with respect to the thickness of some cardiac structures is a key parameter.

Measuring left ventricle (LV) thickness is very important in the context of ischemic and nonischemic cardiomyopathies where ventricular remodeling occurs, either by thinning or thickening of the LV wall. On one hand, the recent work by Merino-Caviedes et al. [25] suggests that the area affected by thin layers of subendocardial scar substrate correlate better with the cycle length of spontaneous episodes of ventricular tachycardia than the total scar volume in patients with established ischemic cardiomyopathy. On the other, diagnosis of hypertrophic cardiomyopathy is based on detecting LV wall thickness greater than 15 mm in one or more myocardial segments, unexplained by loading conditions [5].

On the right cardiac chambers, right ventricular (RV) wall thickness measured on computed tomography angiography seems to correlate with the pulmonary arterial obstruction index and both were highly predictive of in-hospital mortality in patients with pulmonary embolism [11]. A retrospective analysis of a cohort of patients with pulmonary hypertension, based on echocardiographic studies, concluded that RV relative wall thickness could predict

*Corresponding author

✉ smercav@lpi.tel.uva.es (S. Merino-Caviedes); marcma@tel.uva.es (M. Martín-Fernández); terper@wmatem.eis.uva.es (M.T. Pérez Rodríguez); migmar@tel.uva.es (M.Á. Martín-Fernández); david.filgueiras@cnic.es (D. Filgueiras-Rama); fedsim@tel.uva.es (F. Simmross-Wattenberg); caralb@tel.uva.es (C. Alberola-López)

ORCID(s): 0000-0002-4689-9766 (S. Merino-Caviedes); 0000-0001-9342-9989 (M. Martín-Fernández); 0000-0002-6313-9443 (M.Á. Martín-Fernández); 0000-0001-5909-2454 (D. Filgueiras-Rama); 0000-0001-9534-1016 (F. Simmross-Wattenberg); 0000-0003-3684-0055 (C. Alberola-López)

[1]Full affiliation of Dr. Filgueiras-Rama: Centro Nacional de Investigaciones Cardiovasculares (CNIC). Novel Arrhythmogenic Mechanisms Program. Madrid, Spain. Instituto de Investigación Sanitaria del Hospital Clínico San Carlos (IdISSC), Cardiovascular Institute. Madrid, Spain. Centro de Investigación Biomédica en Red de Enfermedades Cardiovasculares (CIBERCV). Madrid, Spain.

mid-term RV reverse remodeling after treatment, and was associated with long-term outcomes [32]. RV wall thickness of more than 5 mm is a marker of disease progression [36]. A recent meta-analysis has also compiled evidence showing that severe cases of COVID-19 often show RV dysfunctions that may take the form of a specific radial, instead of longitudinal dysfunction, and that it is commonly accompanied by RV dilation due to pressure overload [8]. In addition, a recent multicenter study [35] reported an independent association between RV dysfunction and one-year mortality in hospitalized patients with COVID-19. Unlike other imaging modalities, late-gadolinium enhanced (LGE) CMR allows to simultaneously assess myocardial scarring on right ventricular regions [28]. Measuring right ventricular wall thickness poses additional challenges compared to the LV, that stem from the facts that the RV is thinner than the LV wall, its shape varies more than the LV and its insertions on the LV septum may not be well defined and, as in the LV, there are trabeculae and papillary muscles at the RV endocardium ([40], [29], [27]).

Other anatomical targets have been reported where measuring thickness is of interest, using either MR or other imaging modalities; specifically, we may mention the brain cortex [18], the heart atria [38], articular cartilage [33], intracranial arteries [17], the carotid bulb [2] or the gallbladder [30] to cite some of them.

Generally speaking, thickness may be defined as the distance between two appropriately selected points on opposite boundaries. However, there is no consensus in the literature with respect to how to choose these points or whether to measure the distance as a segment length in an Euclidean sense or adding more involved concepts like the Geodesic distance. Concerning thickness measurement, some methods use geometric-based point correspondences such as, for example, tracing a ray along the normal vector of a surface to the other [33]. In short-axis slices of the LV, thickness has been measured by means of rays that follow the local normal of the centerline between both boundaries [34] or assuming the wall to have radial symmetry and tracing rays along the radial direction from a chosen center [26].

Finding point correspondences for ray-tracing, however, may not be unique or invertible, as was pointed out in [18]. Specifically, in this reference Jones *et al.* proposed to solve the Laplace equation with Dirichlet boundary conditions to set up unique point to point correspondences between surfaces, and many references therein have adopted this philosophy, which is especially suitable when the domain boundaries are curved. This methodology has proved to be more reproducible than projecting rays along normal vectors from one boundary to the opposite, as reported in [30] or [20]. This method continues to be utilized in recent research to calculate thickness, such as [19]. Also, a recent method [4] to compute maximum wall thickness of the LV on hypertrophic cardiomyopathy achieved lower test-retest error than human experts by segmenting the LV myocardium on CMR images using a U-Net network and then computing distances using the Laplace equation to find correspondences between points. A possible explanation for this is that, for human experts, choosing the points on the boundaries is a non-straightforward task, prone to uncertainty. In [24], the Multi-Stencil Streamline Fast Marching (MS-SFM) method was proposed to generate thickness maps of the LV wall and, if desired, of the myocardial scar, using partial differential equations. The Laplace equation was utilized to establish correspondences between the LV endocardium and epicardium but the streamlines were not explicitly computed.

The classic finite difference methods to solve the Laplace equation (Jacobi explicit, Gauss-Seidel explicit and implicit) enforce the [Dirichlet] boundary conditions by fixing the value of voxels outside the domain, and contiguous to a domain boundary, to the value provided by the Dirichlet condition [16]. This generates a discretization of the domain boundaries and prevents subvoxel precision when the domain is too thin. Within this context, [15] proposed a methodology based on the Ghost Fluid method [12], where the domain boundaries are defined with subvoxel precision by a level set function. The numerical scheme at voxels within the domain with incomplete neighborhoods (that is, with voxel neighbors outside the domain) uses extrapolated values for the latter. However, the method suffers from instabilities when the boundary is placed too close to a voxel location, so a parameter with the minimum distance allowed between the boundary and a voxel location is introduced. Its implementation uses an implicit scheme where an $N_i \times N_i$ matrix, with N_i the number of nodes in the domain, is built. Although this matrix is sparse, the memory requirements to run this method are very high for relatively large 3D domains. Other methods with higher order of accuracy [13, 14] also require a wider stencil for the numerical scheme, which makes them unsuitable for thin domains such as the RV wall. In [10], [3] and [9], the problem is solved by setting up a linear system of $N_i + N_g$ unknowns, with N_g the number of ghost nodes. This linear system was considered the steady state of an evolutionary problem with a fictitious time, which was solved using a multigrid strategy given the high computational cost of the method. However, its L_1 error norm was significantly higher than the one committed by [15] (2.5 to 3 times higher). This was attributed [10] to defining only one value to each ghost node, whereas [15] could use several values for a ghost node.

In this paper we provide a framework to compute thickness on irregularly-shaped thin walls. We bear in mind the problem of calculating the width of the RV, although we pose it as a general framework to calculate thickness between two close-by non-intersecting surfaces, where one of them is enclosed by the other. Our main contribution is an algorithm to solve the Laplace equation that uses ghost nodes and is able to extrapolate values on them. To avoid the high memory requirements of implicit methods in 3D domains, our proposal is implemented as an iterative algorithm that uses an explicit scheme on voxels with complete neighborhoods and a new semi-implicit scheme on voxels immediately contiguous to the domain. By solving a local linear system of equations to

S. Merino-Caviedes, M. Martín-Fernández, M. T. Pérez Rodríguez, M. Á. Martín-Fernández, D. Filgueiras-Rama, F. Simmross-Wattenberg, C. Alberola-López: *Preprint submitted to Elsevier*

Page 2 of 14

update the value at each contiguous node, the problem of instabilites suffered by [15] is avoided. After the solution within the domain has converged, the values at the ghost nodes are computed using a different least squares problem. Thanks to the extrapolated values on the ghost nodes, the domain where thickness is measured may be extended one voxel beyond the boundary. Thickness values are computed by tracing streamlines from the outer surface (in our case, the epicardium) to the inner surface (the endocardium) and computing their length. The method is tested on a mathematical phantom, the biventricular segmentations of the CMR acquisitions of ten pigs and the RV Segmentation Challenge dataset [29], and it improves the mean L_1 error norm of the thickness measurements over state of the art methods at least 43.28%. In addition, the method surpasses other state of the art methods in classifying RV myocardial segments depending on the RV wall thickness, especially in the detection of thin segments.

The rest of the article is structured as follows. Section 2 describes the proposed local semi-implicit method to solve the Laplace problem. In Section 3, the materials and processing pipeline to apply the previous methods to compute the RV thickness maps are described. Experimental results are shown in Section 4 and discussed in Section 5.

2. Locally Semi-Implicit Scheme with Extrapolation

2.1. Formulation of the Laplace Problem

Let $\Omega \subset \mathbb{R}^{N_d}$ be an N_d-dimensional domain where an isotropic grid is defined. The spacing between contiguous nodes along the i-th dimension is h_i. Let $\mathbf{v}_i = (0, \dots, h_i, \dots, 0)^T$ be a vector that points to the location of the next node in the ith dimension ($\|\mathbf{v}_i\| = h_i$). Let $\Omega_R \subset \Omega$ be the domain enclosed by $\Gamma_0 \subset \Omega$ and $\Gamma_1 \subset \Omega$. In the following, the proposed method intends to find $s : \mathbb{R}^{N_d} \to \mathbb{R}$ that solves the Laplace problem:
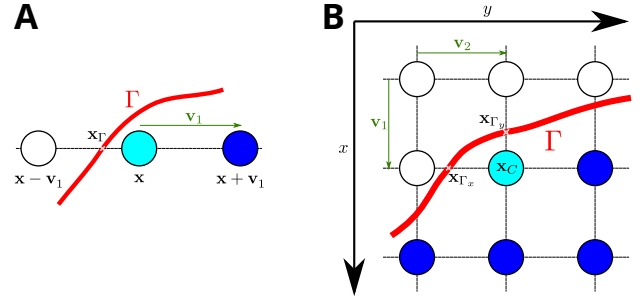
$$\nabla^2 s(\mathbf{x}) = 0 \text{ s.t. } s(\Gamma_0) = s_0, s(\Gamma_1) = s_1 \quad (1)$$

for $\mathbf{x} \in \Gamma_0 \cup \Omega_R \cup \Gamma_1$. Since $s(\cdot)$ is a real-valued, harmonic function and $\Gamma_0 \cup \Omega_R \cup \Gamma_1$ is a connected domain, by the Maximum Principle $s(\cdot)$ can only have a maximum or minimum within Ω_R only if it is constant over the whole domain, and it attains its maximum and minimum values on $\Gamma_0 \cup \Gamma_1$ (see, for example, [6] for proof and further details).

2.2. Linear System for Incomplete Neighborhoods

The values of $s(\cdot)$ on the boundaries are expressed using an auxiliary piecewise constant implicit function $f(\cdot)$ which is built so that $f(\Gamma_0) = s_0$ and $f(\Gamma_1) = s_1$. The boundaries Γ_0 and Γ_1 are also expressed implicitly by means of a signed distance map $\phi(\cdot)$ such that $\phi(\Gamma_0 \cup \Gamma_1) = 0$ and $\phi(\mathbf{x}) < 0$ if $\mathbf{x} \in \Omega_R$ and $\phi(\mathbf{x}) \geq 0$ otherwise. Finally, let $\Gamma = \Gamma_0 \cup \Gamma_1$.

As in other methods, such as [15], the algorithm is described first for an incomplete one-dimensional neighborhood, and it is then extended to higher dimensional neighborhoods. The nodes outside the domain that would complete an

Figure 1: A. Illustration of an one-dimensional neighborhood with one ghost value next to Γ. B. Two-dimensional neighborhood with two ghost values next to Γ.

incomplete neighborhood are called ghost nodes. Figure 1 depicts a neighborhood where the boundary Γ is located between nodes $\mathbf{x} - \mathbf{v}_1$ and $\mathbf{x}$, with $\mathbf{x}_\Gamma$ being the intersection point between Γ and the segment delimited by $\mathbf{x} - \mathbf{v}_1$ and $\mathbf{x}$. Nodes $\mathbf{x}$ and $\mathbf{x} + \mathbf{v}_1$ (in blue) belong to Ω_R, whereas $\mathbf{x} - \mathbf{v}_1$ (in white) does not; therefore, a ghost value $s^G(\mathbf{x} - \mathbf{v}_1)$ is assigned to it.

This way, the second order approximation to the second derivative along $\mathbf{v}_1$ can be built, and the Dirichlet condition for $\mathbf{x}_\Gamma \in \Gamma$ can be established using a second order Lagrange polynomial interpolator $\tilde{s}^I(\cdot)$. From the boundary condition $s(\Gamma_0) = s_0$, the equation $\tilde{s}^I(\mathbf{x}_\Gamma) = s_0$ is obtained, and the following linear system can be established for the neighborhood:

$$\tilde{s}^I(\mathbf{x}_\Gamma) = s^G(\mathbf{x} - \mathbf{v}_1)l_{-1}(\mathbf{x}_\Gamma) + s(\mathbf{x})l_0(\mathbf{x}_\Gamma)$$
$$+ s(\mathbf{x} + \mathbf{v}_1)l_1(\mathbf{x}_\Gamma) = f(\mathbf{x}_\Gamma)$$

$$l_j(\mathbf{y}) = \prod_{\substack{i=-1 \\ i \neq j}}^{1} \frac{\|\mathbf{y} - (\mathbf{x} + i\mathbf{v}_1)\|}{\|(\mathbf{x} + j\mathbf{v}_1) - (\mathbf{x} + i\mathbf{v}_1)\|}, j = -1, 0, 1 \quad (2)$$

where $s^G(\mathbf{x} - \mathbf{v}_1)$ is called a ghost value for $\mathbf{x} - \mathbf{v}_1$, which is outside the domain where $s(\cdot)$ is properly defined. From the discretization of the Laplace equation, we have:

$$\frac{s^G(\mathbf{x} - \mathbf{v}_1) - 2s(\mathbf{x}) + s(\mathbf{x} + \mathbf{v}_1)}{h_1^2} = 0 \quad (3)$$

Equations (2) and (3) can be written as a linear system:

$$\begin{pmatrix} f(\mathbf{x}_\Gamma) \\ 0 \end{pmatrix} = \begin{pmatrix} l_{-1}(\mathbf{x}_\Gamma) & l_0(\mathbf{x}_\Gamma) & l_1(\mathbf{x}_\Gamma) \\ \frac{1}{h_1^2} & \frac{-2}{h_1^2} & \frac{1}{h_1^2} \end{pmatrix} \begin{pmatrix} s^G(\mathbf{x} - \mathbf{v}_1) \\ s(\mathbf{x}) \\ s(\mathbf{x} + \mathbf{v}_1) \end{pmatrix} \quad (4)$$

If we now define

$$\mathbf{b}_\Gamma^\mathbf{x} = \begin{pmatrix} f(\mathbf{x}_\Gamma) & 0 \end{pmatrix}^T$$

$$\mathbf{m}^\mathbf{x} = \begin{pmatrix} l_1(\mathbf{x}_\Gamma) & \frac{1}{h_1^2} \end{pmatrix}^T$$

$$\mathbf{u}_s^{\mathbf{x}} = \begin{pmatrix} s^G(\mathbf{x} - \mathbf{v}_1) & s(\mathbf{x}) \end{pmatrix}^T$$

$$u_k^{\mathbf{x}} = s(\mathbf{x} + \mathbf{v}_1)$$

$$\mathbf{A}^{\mathbf{x}} = \begin{pmatrix} l_{-1}(\mathbf{x}_\Gamma) & l_0(\mathbf{x}_\Gamma) \\ \frac{1}{h_1^2} & \frac{-2}{h_1^2} \end{pmatrix}$$

where T stands for transpose, we can write

$$\mathbf{b}_\Gamma^{\mathbf{x}} = \begin{pmatrix} \mathbf{A}^{\mathbf{x}} & \mathbf{m}^{\mathbf{x}} \end{pmatrix} \begin{pmatrix} \mathbf{u}_s^{\mathbf{x}} \\ u_k^{\mathbf{x}} \end{pmatrix}$$

$$\mathbf{b}_\Gamma^{\mathbf{x}} = \mathbf{A}^{\mathbf{x}} \mathbf{u}_s^{\mathbf{x}} + \mathbf{m}^{\mathbf{x}} u_k^{\mathbf{x}}$$

$$\underbrace{\mathbf{b}_\Gamma^{\mathbf{x}} - \mathbf{m}^{\mathbf{x}} u_k^{\mathbf{x}}}_{b^{\mathbf{x}}} = \mathbf{A}^{\mathbf{x}} \mathbf{u}_s^{\mathbf{x}} \qquad (5)$$

so we end up having a linear system which may be expressed as:

$$\mathbf{A}^{\mathbf{x}} u_s^{\mathbf{x}} = b^{\mathbf{x}} \qquad (6)$$

where $\mathbf{A}^{\mathbf{x}}$ contains coefficients relative to the unknowns $u_s^{\mathbf{x}}$. Vector $b^{\mathbf{x}}$, as introduced in Eq. (5), can be expressed

$$b^{\mathbf{x}} = \mathbf{b}_\Gamma^{\mathbf{x}} - \mathbf{m}^{\mathbf{x}} u_k^{\mathbf{x}} \qquad (7)$$

where $\mathbf{b}_\Gamma^{\mathbf{x}}$ represents the terms that depend on $f(\cdot)$ and $\mathbf{m}^{\mathbf{x}}$ is a vector containing the coefficients applied on $u_k^{\mathbf{x}}$. Notice that $\mathbf{A}^{\mathbf{x}}$, $\mathbf{b}_\Gamma^{\mathbf{x}}$ and $\mathbf{m}^{\mathbf{x}}$ depend only on the geometry of the problem at the neighborhood of $\mathbf{x}$.

When the neighborhood has more than one dimension, we have one equation coming from the discretization of the Laplace equation which will include one or more *Ghost* nodes, and one equation such as (2) for each of the *Ghost* nodes. The scalar quantity $u_k^{\mathbf{x}}$ becomes vector $\mathbf{u}_k^{\mathbf{x}}$ and, correspondingly, vector $\mathbf{m}^{\mathbf{x}}$ becomes matrix $\mathbf{M}^{\mathbf{x}}$. The former will include values of function $s(\cdot)$ to be determined in nodes which are neither ghosts nor node $\mathbf{x}$, and matrix $\mathbf{M}^{\mathbf{x}}$ will include coefficients on these nodes; this matrix, as it was the case of $\mathbf{m}^{\mathbf{x}}$ is 1D, is only a function of the problem geometry. Accordingly, Eq. (7) becomes

$$b^{\mathbf{x}} = \mathbf{b}_\Gamma^{\mathbf{x}} - \mathbf{M}^{\mathbf{x}} \mathbf{u}_k^{\mathbf{x}} \qquad (8)$$

2.3. Algorithm

The method is designed as an iterative method and resembles the Gauss-Seidel explicit method (see, for example, [16]) in that it uses the updated values of nodes already visited at the current iteration. The pseudocode of the full algorithm can be found in Algorithm 1. The inputs are the signed distance map to the boundary contours $\phi(\cdot)$ and $f(\cdot)$. For implementation purposes, $f(\cdot)$ is defined outside Γ such that $f(\mathbf{x})$ is assigned the value of $f(\cdot)$ at the point of Γ closest to $\mathbf{x}$. The first step is to assign to each node in the domain one of the following labels:

- *Far*, if neither the node nor its neighbors are within Ω_R.

- *Ghost*, if the node is not in Ω_R, but at least one of its neighbors is.

- *Contiguous*, if the node is within Ω_R, but at least one of its neighbors is not.

- *Interior*, if both the node and all of its neighbors belong to Ω_R.

where a voxel neighbors refers to the voxels immediately contiguous to it along the grid axes. When all the nodes are labeled, the *Contiguous* nodes are grouped into a set, and the *Interior* nodes are also grouped together. For each *Contiguous* node $\mathbf{x}_C$, $\mathbf{A}^{\mathbf{x}_C}$, $\mathbf{b}_\Gamma^{\mathbf{x}_C}$ and $\mathbf{M}^{\mathbf{x}_C}$ are obtained. $(\mathbf{A}^{\mathbf{x}_C})^{-1}$ can also be computed, in order to speed up the algorithm. For the sake of completeness, panel B of figure 1 shows a 2D neigbourhood of point $\mathbf{x}_C$ in which contour Γ encloses a subset of the grid points. $\mathbf{v}_1$ is considered the vertical direction with grid spacing h_1 and $\mathbf{v}_2$ and h_2 have the same meaning in the horizontal direction. Let $\mathbf{x}_{\Gamma_x}$ be the off-grid contour point in the vertical direction and $\mathbf{x}_{\Gamma_y}$ in the horizontal direction. Then it is easy to obtain the following data structures:

$$\left(\underbrace{\begin{matrix} l_{-1}^{h_2}(\mathbf{x}_{\Gamma_y}) & 0 & l_0^{h_2}(\mathbf{x}_{\Gamma_y}) \\ 0 & l_{-1}^{h_1}(\mathbf{x}_{\Gamma_x}) & l_0^{h_1}(\mathbf{x}_{\Gamma_x}) \\ \frac{1}{h_2^2} & \frac{1}{h_1^2} & -\left(\frac{2}{h_1^2} + \frac{2}{h_2^2}\right) \end{matrix}}_{\mathbf{A}^{\mathbf{x}_C}} \quad \underbrace{\begin{matrix} l_1^{h_2}(\mathbf{x}_{\Gamma_y}) & 0 \\ 0 & l_1^{h_1}(\mathbf{x}_{\Gamma_x}) \\ \frac{1}{h_2^2} & \frac{1}{h_1^2} \end{matrix}}_{\mathbf{M}^{\mathbf{x}_C}} \right)$$

and

$$\mathbf{b}_\Gamma^{\mathbf{x}} = \begin{pmatrix} f(\mathbf{x}_{\Gamma_y}) & f(\mathbf{x}_{\Gamma_x}) & 0 \end{pmatrix}^T$$

$$\mathbf{u}_s^{\mathbf{x}_C} = \begin{pmatrix} s^G(\mathbf{x}^C - \mathbf{v}_2) & s^G(\mathbf{x}^C - \mathbf{v}_1) & s(\mathbf{x}^C) \end{pmatrix}^T$$

$$\mathbf{u}_k^{\mathbf{x}_C} = \begin{pmatrix} s(\mathbf{x} + \mathbf{v}_2) & s(\mathbf{x} + \mathbf{v}_1) \end{pmatrix}^T$$

The initial values of the iteration are set as follows: ghost nodes associated to Γ_0 are given the value s_0 and those associated to Γ_1 the value s_1. Let N_{Γ_0} denote the number of ghost nodes associated to Γ_0 and N_{Γ_1} the corresponding number for Γ_1. Let $f_{mean} = (N_{\Gamma_0} s_0 + N_{\Gamma_1} s_1)/(N_{\Gamma_0} + N_{\Gamma_1})$. *Interior* or *Contiguous* nodes are given the value f_{mean}. Then, on each iteration, the *Contiguous* nodes are updated first and the *Interior* nodes, second. In order to improve the speed of the solution convergence, the nodes of each set are sorted by their value of $\phi(\cdot)$, so that the nodes closest to Γ are updated first. When a *Contiguous* node $\mathbf{x}_C$ is updated, the value of the rest of the nodes in Ω_R is considered fixed. Then, $s^{(m+1)}(\mathbf{x}_C)$ is obtained from $\mathbf{u}_s^{\mathbf{x}_C,(m+1)}$ after solving:

$$\mathbf{u}_s^{\mathbf{x}_C,(m+1)} = (\mathbf{A}^{\mathbf{x}_C})^{-1} \left(\mathbf{b}_\Gamma^{\mathbf{x}_C} - \mathbf{M}^{\mathbf{x}_C} \mathbf{u}_k^{\mathbf{x}_C,(m,m+1)} \right) \qquad (9)$$

where $\mathbf{u}_k^{\mathbf{x}_C,(m,m+1)}$ is composed by the values of the solution at iteration (m) or $(m+1)$, depending on the node visit plan. After all the contiguous nodes are updated, the *Interior* nodes are visited, and its values are computed using:

$$s^{(m+1)}(\mathbf{x}) = \frac{\displaystyle\sum_{i=1}^{N_d} \frac{s^{(m,m+1)}(\mathbf{x}+\mathbf{v}_i) + s^{(m,m+1)}(\mathbf{x}-\mathbf{v}_i)}{h_i^2}}{\displaystyle\sum_{i=1}^{N_d} \frac{2}{h_i^2}} \qquad (10)$$

Notice that ghost nodes can be updated by solving Eq. (6). However, this has no relevance for the iterations. Ghost nodes are treated as described in Section 2.4.

Input: $\phi(\mathbf{x})$, $f(\mathbf{x})$, $\forall \mathbf{x} \in \Omega$
Generate label map
  $L(\mathbf{x}) : \Omega \rightarrow \{Far, Ghost, Contiguous, Interior\}$
Build and sort the *Contiguous* and *Interior* subsets
forall $\{\mathbf{x}_C | L(\mathbf{x}_C) = Contiguous\}$ **do**
  | Compute $\mathbf{A}^{\mathbf{x}_C}$, $\mathbf{b}_\Gamma^{\mathbf{x}_C}$ and $\mathbf{M}^{\mathbf{x}_C}$
end
$s^{(0)}(\Omega_R) = f_{mean}$, $m = 0$
repeat
  | **forall** $\{\mathbf{x}_C | L(\mathbf{x}_C) = Contiguous\}$ **do**
  | | $\mathbf{b}^{\mathbf{x}_C,(m)} = \mathbf{b}_\Gamma^{\mathbf{x}_C} - \mathbf{M}^{\mathbf{x}_C} \cdot \boldsymbol{u}^{(m)}$
  | | Compute $s^{(m+1)}(\mathbf{x}_C)$ using (9)
  | **end**
  | **forall** $\{\mathbf{x}_I | L(\mathbf{x}_I) = Interior\}$ **do**
  | | Compute $s^{(m+1)}(\mathbf{x}_I)$ using (10)
  | **end**
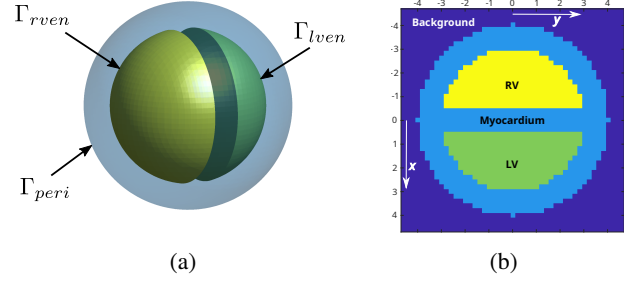 | $m = m + 1$
until *Convergence*

Algorithm 1: Pseudocode of the proposed method to solve the Laplace problem.

2.4. Extension of the Solution to Ghost Nodes

There are situations in which it is desirable to extrapolate values to the ghost nodes, such as extending the computation of the thickness maps by one voxel to provide better estimations of the thickness on Γ_1. In such a case, the straightforward alternative would be to keep the values of the ghost nodes computed along with the values of the *Contiguous* nodes using (9). However, if a *Ghost* node takes part in the computation of more than one *Contiguous* node, this strategy will make the *Ghost* node depend only on the *Contiguous* node system last visited. For this reason, we extend the solution at the *Ghost* nodes by considering the value of the *Contiguous* and *Interior* nodes as fixed and the values of all the *Ghost* nodes as the unknowns $\mathbf{u}^G$ of a linear system of equations, which is solved as the following linear least squares problem with linear inequality constraints to enforce the monotonicity of the solution outside Ω_R:

$$\min_{\mathbf{u}^G} \frac{1}{2}\|\mathbf{A}^{LS}\mathbf{u}^G - \mathbf{b}^{LS}\|^2 \text{ s.t. } \mathbf{C}\mathbf{u}^G \leq \mathbf{d}^G \qquad (11)$$

The extrapolation linear system $\mathbf{A}^{LS}\mathbf{u}^G = \mathbf{b}^{LS}$ is built with the equalities as in Eq. (6) for the whole set of *Contiguous* nodes. $\mathbf{A}^{LS}$ is a matrix with N_{LS} rows, one for each equation of the local linear systems for updating the *Contiguous* nodes, and N_G columns, with N_G the number of ghost nodes. The independent terms of the local linear systems are updated with the solution after it has converged,

(a)   (b)

Figure 2: (a) Surfaces of the myocardial borders and (b) XY slice of the discretization of the phantom with parameters $R_1 = 3$, $R_2 = 4$, $L = 1$ and $h = 0.2$.

$s^{m^*}(\cdot)$. Also, the elements of $\mathbf{A}^\mathbf{x}\boldsymbol{u}_s^\mathbf{x}$ that depend on the solution at *Contiguous* nodes are moved to vector $\mathbf{b}^{LS}$ after computing its numerical value using $s^{m^*}(\cdot)$. Regarding the linear inequality system $\mathbf{C}\mathbf{u}^G \leq \mathbf{d}^G$, $\mathbf{C}$ is a diagonal $N_G \times N_G$ matrix whose diagonal elements take the values $\{-1, 1\}$ depending on whether the extrapolated value needs to be over or below, respectively, the Dirichlet boundary condition given through $f(\cdot)$. Accordingly, the values of $\mathbf{d}^G$ take the values of $f(\cdot)$ where the extrapolated values need to be below the Dirichlet condition, and $-f(\cdot)$ otherwise. Problem (11) is solved using the Matlab Optimization Toolbox.

The methodology presented in this section will be hereinafter referred to as Locally (semi) IMplicit method with EXtrapolation (*limex*) to the ghost nodes. This scheme is semi-implicit because on the linear systems built for the *Contiguous* nodes, not all the neighborhood nodes are unknowns, as in implicit schemes, but more nodes than the central one $\mathbf{x}_C$ are unknowns, unlike explicit schemes. The solution space in which function $s(\cdot)$ is calculated (including the ghost nodes) will be hereinafter referred to as Ω_V. Ω_V depends on the grid discretization and $\Omega_V \rightarrow \Gamma_0 \cup \Omega_R \cup \Gamma_1$ as $h \rightarrow 0$.

3. Materials and Methods

3.1. Materials

3.1.1. Numerical Phantom

A phantom with variable wall thickness and grid spacing was used to test the methodology. This phantom needed to be sufficiently simple so that analytical thickness measures could be employed but, simultaneously, its configuration should also be sufficiently similar to the biventricular mask. The chosen phantom consists of an outer sphere of radius R_2 resembling the pericardium (Γ_{peri}) and two symmetric spherical caps of an inner concentric sphere of radius R_1, one for the LV endocardium (Γ_{lven}) and the other for the RV endocardium (Γ_{rven}). The spherical cap planes are parallel to the YZ plane and cut the x-axis on $\{-L/2, L/2\}$. Fig. 2(a) contains an instance of the phantom surfaces. The phantom dataset will be made available upon reasonable request.

3.1.2. Dataset of Real RV Segmentations from Pigs

This dataset contains the segmentation of the biventricular myocardium of ten pigs with established myocardial infarction, delineated on high resolution 3D LGE-CMR images. All procedures in pigs were approved by the Centro Nacional de Investigaciones Cardiovasculares (CNIC) Committee on Use and Care of Animals and by the Comunidad de Madrid (Ref#PROEX097/17). Animal experiments comply with Spanish (RD53/2013, ECC/566/2015),

---

European (2010/63/EU) and Animal Research: Reporting of In Vivo Experiments (ARRIVE) guidelines. The images were acquired with a Philips Achieva 3T-Tx whole-body scanner equipped with a 32-element and phased-array cardiac coil (Philips Healthcare, Best, The Netherlands), using an inversion-recovery spoiled turbo field echo (IR-T1TFE) with isotropic resolution of $1.5 \times 1.5 \times 1.5$ mm (reconstruction resolution $0.57 \times 0.57 \times 0.75$ mm). An initial segmentation of the biventricular wall was obtained semi-automatically with custom-made software in Matlab, which served as a basis for a fine manual segmentation done by cardiologists (8-12 h per segmentation). Further details can be found in [25]. The segmentations, which include papillary muscles, were provided as surface triangulations. In Panel A of Fig. 8, one of these surface triangulations is shown. The pig dataset will be made available upon reasonable request.

3.1.3. RV Segmentation Challenge Data

The dataset of the Right Ventricle Segmentation Challenge (RVSC), held at the MICCAI'12 Conference, is publicly available at https://rvsc.projets.litislab.fr/ (accessed: 2023-02-28). It contains data from 48 patients who were referred to the Rouen University Hospital for a cardiac MR examination. Clinical indications included myocarditis, ischaemic cardiomyopathy, suspicion of arrhythmogenic right ventricular dysplasia, dilated cardiomyopathy, hypertrophic cardiomyopathy and aortic stenosis [29]. For each patient, a CINEmatic short-axis image was provided, acquired using a retrospectively synchronized balance steady-state free precession sequence on a 1.5T Symphony Tim scanner (Siemens Medical Systems). Sequence parameters were TR = 50 ms, TE = 1.7 ms, flip angle = 55°, slice thickness = 7 mm, space between slices = 8.4 mm and 20 slices per cardiac cycle [29]. Acquired in-plane spatial resolution is 1.6 mm but, after zooming and cropping, reconstructed in-plane spacing varies between 0.57 mm and 0.97 mm. Also, an expert provided manual delineations of the RV endocardium and epicardium on a set of short-axis slices at end-diastole and end-systole for each patient. Experts were asked to consider papillary muscles as part of the ventricular cavity. The number of slices with manual delineations varied between 5 and 12 for each patient and cardiac phase. In total, 757 slices contained manual delineations, which are expressed as a list of spatial coordinates (i.e., they are not binary masks). Expressed permission was attained to use these data for the purpose of measuring RV thickness.

3.2. Methods
3.2.1. General Overview of the Proposed Method

As in other methods that employ the Laplace equation to compute thickness for the LV ([18], [24], [4]), the proposed method to compute thickness in the RV is divided into two main steps: the computation of the correspondences between the endocardium and the epicardium by solving the Laplace equation with boundary conditions, and the computation of the thickness maps, in this case by means of streamlines. For the former we need binary masks while for the latter we need a triangular mesh for 3D or contours for 2D. Section 3.2.2 provides details on how these data structures are created. In addition, signed distance maps $\phi(\cdot)$ are computed using [23] to generate the Euclidean distance map and changing signs where needed according to the binary mask.

The computation of the RV thickness has some particularities when the segmentation of the biventricular myocardium is provided. Since the RV wall is inserted into the LV at the septum, there is some uncertainty about the RV limits, which are also irregularly shaped. In that situation, the right and left ventricles need to be identified beforehand. Also, at some regions, the RV wall is very thin in terms of number of voxels within the wall. Section 3.2.3 provides deeper insight on this topic

3.2.2. Meshes and Binary Masks

The phantom is discretized using an isotropic grid of spacing h and a label map where the background, the biventricular myocardium and the LV and RV cavities are identified. R_1, R_2, L and h are considered measured in mm. Fig. 2(b) contains a slice of the discretized phantom in Fig. 2(a). In addition, we generate a mesh of the phantom as for streamline calculation.

Masks for the RSVC dataset are straightforward to handle since data are processed in 2D. In addition, since contours are provided directly for the RV, no further processing is needed. For terminological simplicity, terms like *vertices* or *triangulation* will be loosely used both for 2D and 3D since for our purposes they are functionally similar.
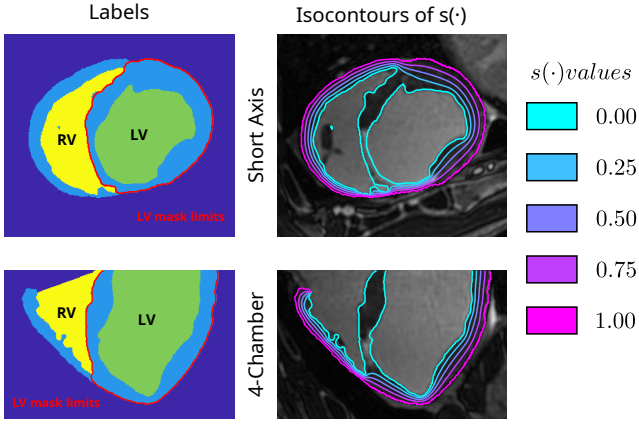
The pig dataset deserves further attention. For each pig, an isotropic 3D grid was generated for each of the following spacings (in mm) $h = 0.4, 1.0, 1.5, 2.0$. Every grid was oriented following the short-axis convention. The spacing $h = 0.4$ mm was employed to generate a silver standard against which to measure the thickness computed on the grids with $h = \{1.0, 1.5, 2.0\}$ mm (further details are provided in Sections 3.2.6 and 4.2). An additional isotropic grid with $h = 0.57$ mm was generated in the same short-axis orientation. This grid is then downsampled in the through-plane dimension to create an anisotropic grid; downsampling factors ranged from 2 to 14, the latter having a space between slices of approximately 8 mm. Then, a binary mask of the biventricular wall was generated on each of the grids by rasterizing the biventricular wall mesh using external software [1]. On each short-axis slice of the biventricular mask, the LV and RV cavities are identified by comparing the slice with the result of applying a hole filling algorithm (available in Matlab). Coherence along the long axis was enforced by analyzing the 3D connectivity of the cavities on the stack of slices. Each triangle within the biventricular surface triangulation was assigned to Γ_{peri}, Γ_{lven} or Γ_{rven} by performing a custom region growing algorithm on the triangulation. Γ_{rven}, Γ_{lven} and Γ_{peri} are the RV endocardial, LV endocardial and pericardial surfaces, respectively. The RV cavity binary mask is refined using the rasterization of Γ_{rven}, to improve its definition at the most basal and apical slices.

3.2.3. Identification of the Right and Left Ventricles Boundary

To identify the border between the RV and the LV, the method described in the supplementary material of [25] is used, where the full of the method can be found. For self-containment purposes, a brief description is provided. A first approximation for the LV mask is built by, first, solving the following problem:

$$\nabla^2 \hat{s}(\mathbf{x}) = 0 \text{ s.t. } \hat{s}(\Gamma_{lven}) = 0, \hat{s}(\Gamma_{rven} \cup \Gamma_{peri}) = 1, \qquad (12)$$

A binary mask is obtained by thresholding with $\hat{s} < 0.98$, which is then morphologically dilated with a spherical kernel with a radius of two voxels. After dilation, all voxels outside the biventricular myocardium are set to zero. The LV mask is refined by using a variational framework based on [7] where the data-driven terms are built using $\hat{s}(\cdot)$, $\|\nabla \hat{s}(\cdot)\|$ and the RV cavity mask. On the left column of Fig. 3, the LV mask limits for one of the pigs are displayed in red over the anatomical labels.

Figure 3: Short axis and 4–chamber views of both the anatomical labels and $s(\cdot)$ isocontours at $s(\cdot) = 0, 0.25, 0.5, 0.75, 1$ for one of the pigs with grid spacing $h = 1.0$.

3.2.4. Generating the Thickness Maps

Depending on whether the biventricular mask (phantom and pig set) or the RV endocardial and epicardial contours are available, the boundary conditions of the Laplace problem are posed differently. In both cases, the problem is solved with the method described in Section 2.

$$\nabla^2 s(\mathbf{x}) = 0 \text{ s.t. } s(\Gamma_{rven}) = 0, s(\Gamma_{rvepi}) = 1, \qquad (13)$$

where Γ_{rven} and Γ_{rvepi} are the RV endocardium and epicardium, respectively. For the biventricular mask, the problem is modified to:

$$\nabla^2 s(\mathbf{x}) = 0 \text{ s.t. } s(\Gamma_{rven} \cup \Gamma_{lven}) = 0, s(\Gamma_{peri}) = 1, \qquad (14)$$

where Γ_{lven} and Γ_{peri} are the LV endocardial and pericardial surfaces, respectively. Setting the boundary conditions $s(\Gamma_{rven}) = 0$ and $s(\Gamma_{lven}) = 0$ prevents that any point at the RV endocardium be connected to a point on the LV endocardium by a streamline of $s(\cdot)$. By solving the problem at the whole biventricular mask, the RV shape irregularity at the insertion on the LV is overcome. The right side of Fig. 3 shows the isocontours of $s(\cdot)$ on a short-axis slice and a 4-chamber slice of one of the pigs. Nodes outside the domain Ω_V (labeled as *Far* when solving the Laplace problem) and within the RV cavity (and within the LV cavity for (14))) were given a value of $s(\cdot) = -10$ to prevent ∇s to point towards the myocardium at the *Ghost* nodes next to the RV endocardium. Likewise, *Far* nodes located at the background are given a value $s(\cdot) = 10$.

Thickness is computed by tracing streamlines along the normalized gradient of the Laplace solution, $\nabla s / \|\nabla s\|$, starting from the triangulation vertices of the RV epicardium, $\{\mathbf{x}_v\}_{v=1}^{N_t}$, until the streamline reaches the RV endocardium. Each streamline $\gamma_v = \{\mathbf{y}_i^v\}_{i=1}^{N_{\gamma_v}}$ was computed with the Euler integration method (using Matlab 2020a). Thickness at each vertex $\mathbf{x}_v$ was defined as the length of its corresponding streamline γ_v. To increase the quality of the streamlines, they were cleaned of segments with a deviation over $\theta_{\max} = 80°$; if such a segment was detected, the segments after it were removed from the streamline.

To detect where the ending point of the streamline was, the values of $s(\cdot)$ at the streamline points $\{\mathbf{y}_i^v\}_{i=1}^{N_{\gamma_v}}$ were interpolated, and the index j that minimized $|s(\mathbf{y}_j^v) - s_0|$, with s_0 being the value
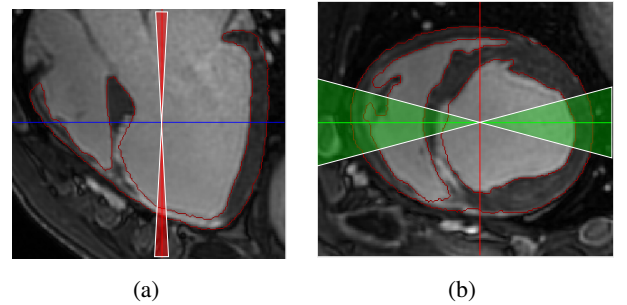
of $s(\cdot)$ at the RV endocardium ($s_0 = 0$), was computed. Then, if $(s(\mathbf{y}_j^v) - s_0)(s(\mathbf{y}_{j-1}^v) - s_0) \le 0$ or $(s(\mathbf{y}_j^v) - s_0)(s(\mathbf{y}_{j+1}^v) - s_0) \le 0$, the end of the streamline is computed as the point within the segment between $\mathbf{y}_j^v$ and $\mathbf{y}_{j\pm1}^v$ where $s(\cdot) = s_0$, assuming that $s(\cdot)$ varies linearly along the segment. Otherwise, if $|s(\mathbf{y}_j^v) - s_0| < \Delta s_{tol}$, $\mathbf{y}_j^v$ is considered the ending point of γ_v. If not, we assume that the streamline has not reached the RV endocardium and the process is repeated after extending γ_v with a new streamline computed from the point $\mathbf{y}_j^v + h_{step} \nabla \phi^{rven}(\mathbf{y}_j^v) / \|\nabla \phi^{rven}(\mathbf{y}_j^v)\|$. ϕ^{rven} is the Euclidean distance map to the RV endocardium.

3.2.5. Data Augmentation

The variability of the pig set and the phantom was increased by reorienting the grid using a rigid transform that simulates the variability that may occur from the manual planning of the short axis orientation. It has the following expression:

$$\begin{aligned} \mathcal{T}(\mathbf{x}, \theta^y, \theta^z, \mathbf{x}^{off}) = & (\mathbf{x}^{gc} - \mathbf{x}_0) - \mathbf{x}^{off} \\ & + \mathbf{R}^z(-\theta^z)\mathbf{R}^y(-\theta^y)(\mathbf{x} - (\mathbf{x}^{gc} - \mathbf{x}_0)) \end{aligned} \qquad (15)$$

where $\mathbf{x}_0$ is the origin of the coordinate system; $\mathbf{x}^{gc}$ is the geometric center of the vertices from the biventricular triangulation (of either the pig or the phantom), which is chosen as the rotation center; $\mathbf{R}^y(\theta^y)$ is a counter-clockwise rotation of angle θ^y around the y-axis; $\mathbf{R}^z(\theta^z)$ is a counter-clockwise rotation of angle θ^z around the z-axis; and $\mathbf{x}^{off}$ controls the translation added to the new grid. Figure 4 illustrates the rotations $\mathbf{R}^y(\theta^y)$ and $\mathbf{R}^z(\theta^z)$ and the ranges for the rotation angles for one of the pigs.

Figure 4: (a) Range (in red) of $\theta^y \in [-3°, 3°]$ for the rotation around the y-axis ($R^y(\cdot)$), and (b) range (in green) of $\theta^z \in [-15°, 15°]$ for the rotation around the z-axis ($R^z(\cdot)$). The y-axis and the z-axis are orthogonal to the image planes in (a) and (b), respectively.

3.2.6. Methods Used for Comparison

Limex is compared with the following thickness computation methods. The method *jones* consists in solving the Laplace problem using the explicit Gauss-Seidel method, computing streamlines with the Euler integration method (using the Matlab 2020a software) from the triangulation vertices of the RV epicardium and returning the length of the streamline as the thickness at that vertex. This is the approach followed in [18]. Methods *impli* and *gibou* only differ from *jones* in the method used to solve the Laplace equation: the implicit method and the ghost nodes method proposed in [15]. Other ghost node based schemes such as [14] and [13] have not been considered since their schemes require the domain to be at least 3 and 4 nodes wide, respectively, along each dimension. Method *mssfm* is the Multi-Stencil Streamline Fast

S. Merino-Caviedes, M. Martín-Fernández, M. T. Pérez Rodríguez, M. Á. Martín-Fernández, D. Filgueiras-Rama, F. Simmross-Wattenberg, C. Alberola-López: *Preprint submitted to Elsevier*

Page 7 of 14

Marching method (MS-SFM) proposed in [24], which is based on partial differential equations; this method generalizes the one described in [39] and provides more accurate results. The thickness maps yielded by *mssfm* are interpolated at the triangulation vertices so that pointwise comparisons with the other methods can be made. Finally, the method *augusto* is computed as *jones*, but the thickness is given as the distance between both streamline endpoints, as in [4]. In total, six thickness methods are considered.

Comparison is based on the quantification of the thickness deviation with respect to the reference solution. For the case of the phantom the reference is straightforward since an analytical solution is available. For each of the two other datasets this role is played by a silver standard (SS), which is built by averaging the solutions of the methods previously described when they are applied on the grid with highest resolution. Details of each of the silver standards are provided in Sections 4.2 and 4.3. Given the reference, we calculate at each vertex of the triangulation of the RV epicardium the absolute deviation of the thickness for each method and the reference. The L_1 and the L_∞ norms of the absolute deviations are employed as metrics:

$$L_1(t, t^{\text{ref}}) = \frac{1}{N_t} \sum_{n=1}^{N_t} |t_n - t_n^{\text{ref}}| \qquad (16)$$

$$L_\infty(t, t^{\text{ref}}) = \max_{n=1,\dots,N_t} (|t_n - t_n^{\text{ref}}|) \qquad (17)$$

where t and t^{ref} are two vectors of the same number N_t of elements containing, respectively, the estimated thickness measurements and their associated reference values.
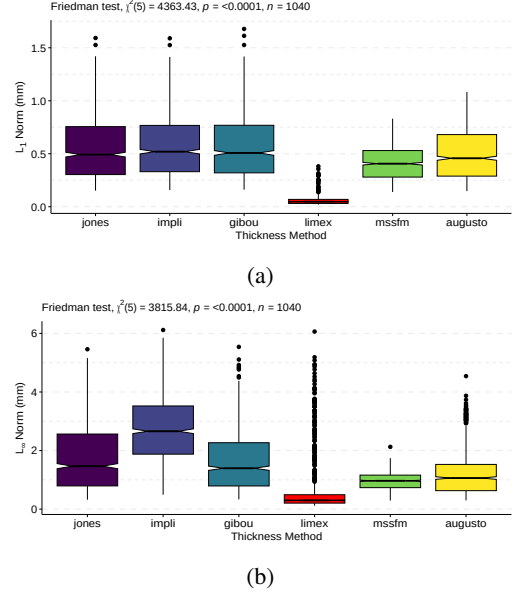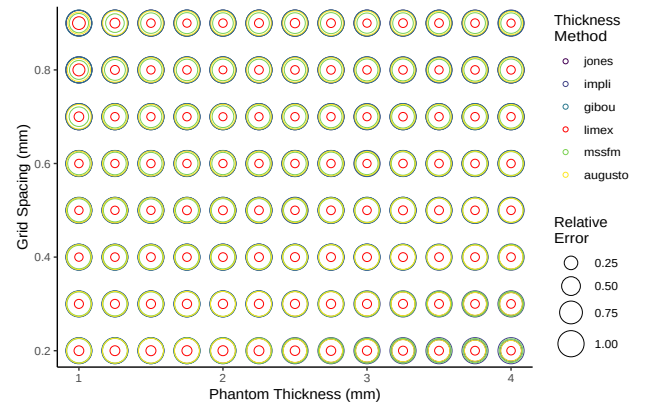
4. Experiments

4.1. Phantom

A total of 104 combinations of parameters for the phantom described in Section 3.1.1 (and Fig. 2) were issued fixing $R_1 = 3$ and $L = 1$, and using every combination of R_2 and h values within the sets $R_2 = \{4 + 0.25i\}_{i=0}^{12}$ and $h = \{0.2 + 0.1j\}_{j=0}^{7}$. For each combination of parameters, the phantom was discretized on ten different grids, each of them the result of applying a rigid transform $\mathcal{T}(\theta^y, \theta^z, \mathbf{x}^{\text{off}})$ with values for θ^y, θ^z and each component of $\mathbf{x}^{\text{off}}$ generated with uniform distributions in the intervals $[-3, 3]$ degrees, $[-15, 15]$ degrees and $[-h/2, h/2]$. The ranges of θ^y and θ^z are illustrated in Figure 4. In total, 1040 instances of the phantom were generated.

Figure 5 contains the boxplots of the L_1 and L_∞ norms of the thickness maps yielded by each of the methods for the 1040 phantom instances. It may be observed that the proposed *limex* method yields, in general, values significantly lower for both norms. The mean L_1 norm for *limex* was 0.055, which was between 86.52% and 90.25% lower than for the rest of the methods. A Friedman test was conducted for each of the norms to detect statistical differences between methods, which were found for both norms with $p < 10^{-4}$. A *post hoc* analysis using the pairwise paired Wilcoxon test with Bonferroni correction for the p-values found statistically significant differences between every pair of methods.

To gain further insight, for each combination of (h, R_2) and per thickness calculation method, the root mean square (RMS) of a 10-element sample of the L_1 values was computed; each element comes from each of the grids defined above. For each (h, R_2), the RMS values were normalized by the maximum RMS value along

(a)

(b)

Figure 5: Boxplot of (a) the L_1 error norms and (b) the L_∞ error norms of the thickness values at the RV epicardium, of the 1040 phantom instances, grouped by the thickness method employed.

Figure 6: Scatter plot where the circle size is scaled by the RMS of all the L_1 norms for each thickness method and phantom instance (smaller means better). Circles are located by the phantom thickness and grid spacing.
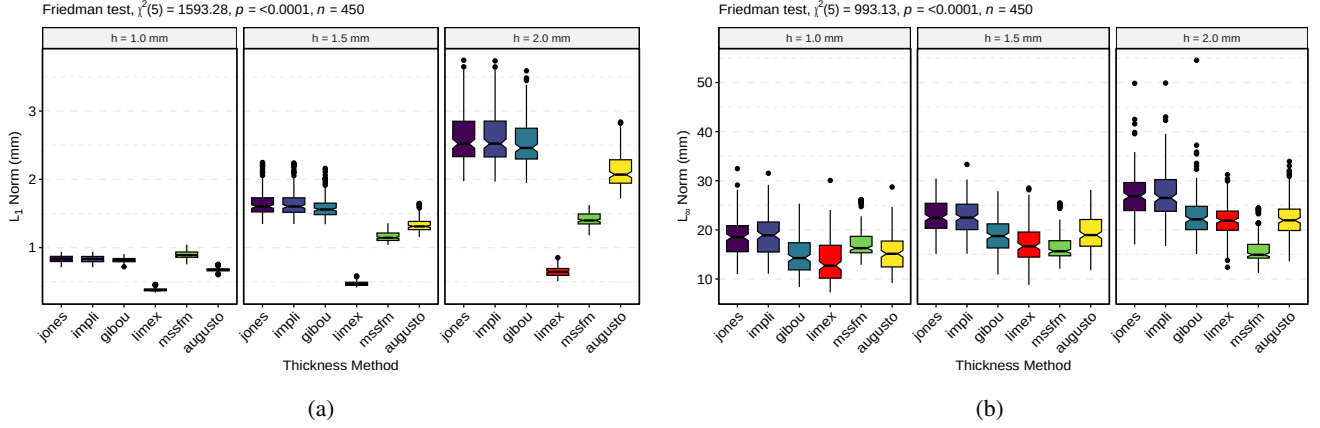
each thickness calculation method. Figure 6 displays a 2D graphical representation of these values as a function of the grid spacing h and the phantom thickness $R_2 - R_1$; specifically, the area of each circle is scaled by the aforementioned ratio (smaller symbol means better method). It can be observed that the *limex* achieves the lowest RMS value for every combination of grid spacing and phantom thickness, whereas the rest of the methods are generally very close to each other.

4.2. Right Ventricular Thickness on Pigs
4.2.1. *Performance on fine-to-coarse isotropic voxels*

The experimental design for the pig data bank was similar to that of the phantoms. For each element on the pig data bank, three grid resolutions were considered: $h = 1.0, 1.5, 2.0$ mm. For each combination of pig and spatial resolution, fifteen different isotropic

S. Merino-Caviedes, M. Martín-Fernández, M. T. Pérez Rodríguez, M. Á. Martín-Fernández, D. Filgueiras-Rama, F. Simmross-Wattenberg, C. Alberola-López: *Preprint submitted to Elsevier*

Page 8 of 14

Figure 7: Boxplot of (a) the L_1 error norms and (b) the L_∞ error norms of the thickness values at the RV epicardium, of the 450 pig instances, grouped by grid spacing and by the thickness method employed.

grids were obtained by applying a rigid transform $\mathcal{T}(\theta^y, \theta^z, \mathbf{x}^{\text{off}})$ to the original short-axis coordinate system and scaling the axes to the chosen spatial resolution. As with the phantoms, θ^y, θ^z and each component of $\mathbf{x}^{\text{off}}$ were generated with uniform distributions in the intervals $[-3, 3]$ degrees, $[-15, 15]$ degrees and $[-h/2, h/2]$, respectively. In total, 450 instances were generated. For each of them, the thickness maps (*jones*, *impli*, *gibou*, *limex*, *mssfm* and *augusto*) were computed. Execution times for *limex* at $h = 1.0$ mm were 118.9 s (98.7 s, 139.1 s), formatted as median (25th percentile, 75th percentile), slightly higher than the other methods; the *gibou* method, for instance, has a median value equal to 91.9 s.

Given that the true myocardial thickness is unknown, a silver standard was generated by using a higher resolution grid. This validation approach has already been used in [17], where the thickness from a high resolution acquisition is considered the ground truth for a corresponding low resolution acquisition. For each pig, the silver standard was computed by upsampling the geometries to a high resolution grid with spacing ($h = 0.4$ mm), computing a thickness map on the upsampled geometry for each of the considered methods (*jones*, *impli*, *gibou*, *limex*, *mssfm* and *augusto*) and averaging, at every triangulation vertex, the interpolated values of those thickness maps. For grid spacings below $h = 0.4$ mm, the *impli* and *gibou* methods could not be computed because they required more memory than the available in our server (484 GB). At resolution $h = 0.4$ mm and for the pig with the largest myocardium, the peak memory consumption (including that of Matlab itself) by the methods that use ghost nodes was 274.02 GB and 13.35 GB for *gibou* and *limex*, respectively, whereas the *jones* method uses 12.03 GB. This sets *limex* as more efficient than *gibou* by a factor of 20.53 and less efficient than *jones* by just a factor of 1.11. Intraclass Correlation Coefficient (ICC) values of the agreement between the six thickness maps, for each pig, were in the interval [0.6580, 0.7830], using the formula ICC(A,1) from [22]. The ICC computed only for the 4 streamline-based methods that consider thickness as the streamline length were in the range [0.9727, 0.9838].

Figures 7(a) and 7(b) show the boxplots of the L_1 and L_∞ norms of the error with respect to the SS, respectively, grouped by the grid resolution. Again, the *limex* method yields the lowest mean L_1 values for every grid resolution: 0.384 mm, 0.474 mm and 0.646 mm for $h = 1.5, 2.0$ mm, respectively, which was between 43.28% and 75.44% lower than the rest of the methods. It also attains the lowest mean L_∞ at $h = 1.0$ mm and the second lowest

at $h = 1.5, 2.0$ mm, with the *mssfm* method being the lowest. Comparing Fig. 7(a) with Fig. 5(a) it turns out that the behavior of the L_1 norm with the pig data at each of the grid resolutions is very similar to the results with the phantoms, in spite of the relatively poor agreement between the thickness maps at $h = 0.4$ mm that take part in the generation of the silver standard.
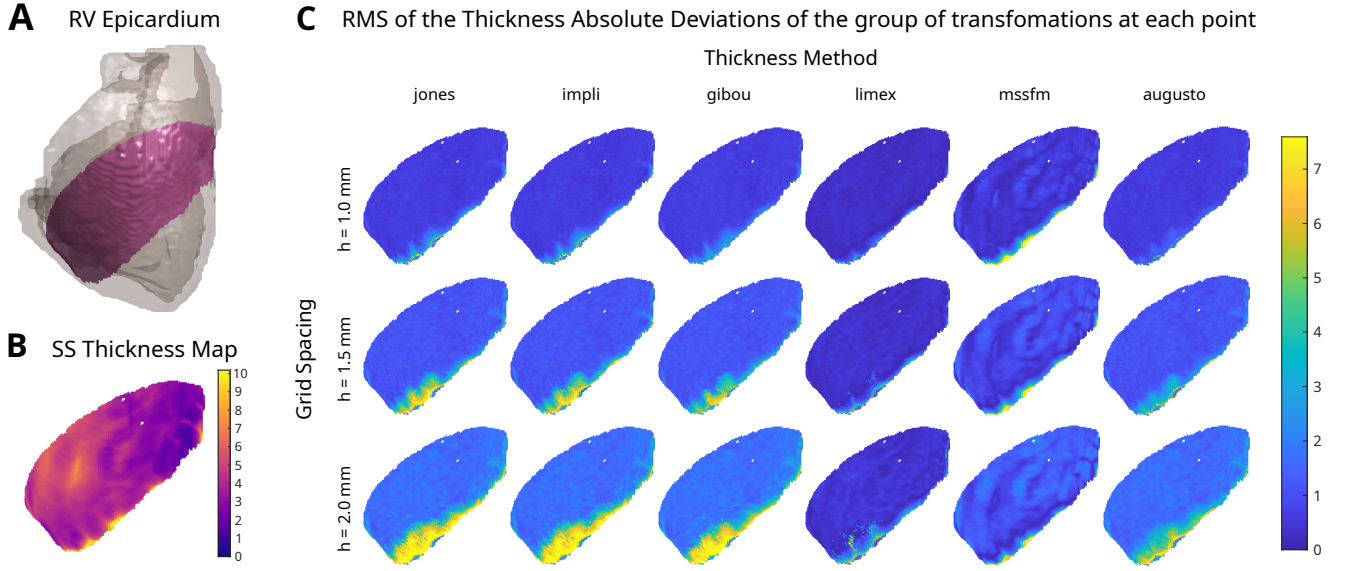
A Friedman test was applied to both the L_1 and the L_∞ norm values to detect statistical differences between the thickness computation methods, and the null hypothesis was rejected for both norms with $p < 10^{-4}$. Then, for each norm and grid resolution, a *post hoc* analysis using the pairwise paired Wilcoxon test with Bonferroni correction for the p-values was performed. There were statistical differences between *limex* and every other method for the L_1 norm. For the L_∞ norm, *limex* was also statistically different from every other method except *mssfm* at $h = 1.5$ mm and *gibou* and *augusto* at $h = 2.0$ mm. Interestingly, statistical differences were found between *jones* and *augusto* on both norms and every grid resolution.

Panel C of Fig. 8 contains the RMS of the absolute deviations with respect to the SS thickness map (which is shown in panel B of the same figure) of the 18 thickness maps computed with the same thickness method and grid resolution, for one of the pigs. It may be observed that the RMS values for the *limex* method increase much less than the rest of the methods as the grid becomes coarser. The border of the RV epicardium closest to the ventricular apex appears to be the region where the error is higher, especially using the coarsest grid. However, methods *limex* and *mssfm* appear to yield the lowest error at that region.
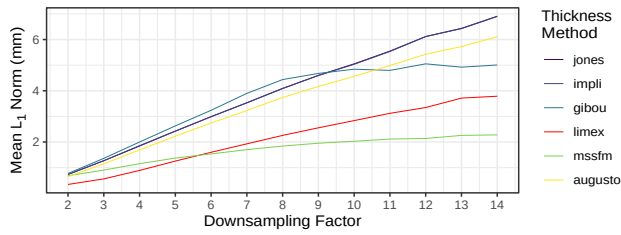
4.2.2. Performance on fine-to-coarse anisotropic voxels

The effect of voxel anisotropy was studied by downsampling the data in the through-plane direction, using integer downsampling factors $n_\downarrow = 2, 3, \ldots, 14$ to generate short-axis oriented grids of resolution $0.57 \times 0.57 \times 0.57 n_\downarrow$ mm. For each pig and downsampling factor combination, five different grids were generated by applying a rigid transform $\mathcal{T}(\theta^y, \theta^z, \mathbf{x}^{\text{off}})$, where the values of θ^y, θ^z and $\mathbf{x}^{\text{off}}$ were generated randomly within the intervals indicated in Section 4.2.1. Then, for each downsampled instance and thickness method, a thickness map was computed and interpolated at the vertices of the RV epicardium, as in Section 4.2.1.

Figure 9 shows the average of the L_1 error norms by thickness method and downsampling factor $n_\downarrow$. As expected, increasing the

S. Merino-Caviedes, M. Martín-Fernández, M. T. Pérez Rodríguez, M. Á. Martín-Fernández, D. Filgueiras-Rama, F. Simmross-Wattenberg, C. Alberola-López: *Preprint submitted to Elsevier*

Page 9 of 14

A RV Epicardium

C RMS of the Thickness Absolute Deviations of the group of transfomations at each point

B SS Thickness Map

Figure 8: A. RV epicardium of one of the pigs. B. Myocardial thickness employed as silver standard ($h = 0.4$ mm). C. RV epicardium colored by RMS of the local absolute deviations of the 15 rigid transformations committed with each thickness method and grid resolution.
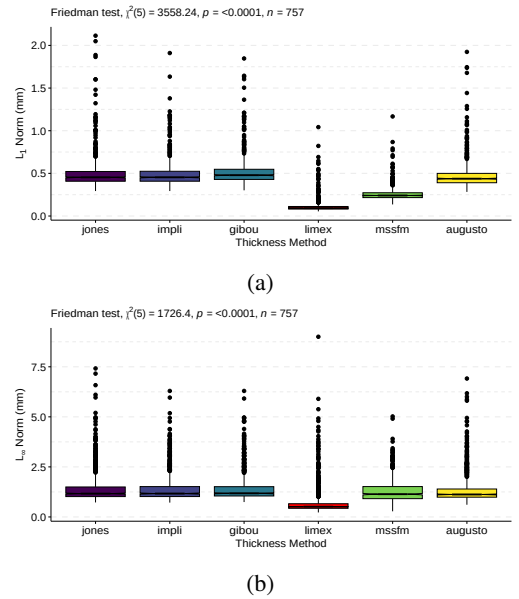

Figure 9: Mean L_1 norm by thickness method and downsampling factor of the anisotropic downsampled pig dataset.

voxel anisotropy increases the error of the thickness measurements. Up to $n_{\downarrow} = 5$, *limex* yields the lowest errors and, for $n_{\downarrow} > 5$, *mssfm* shows more robustness to voxel anisotropy than the other methods.

4.3. RVSC Data
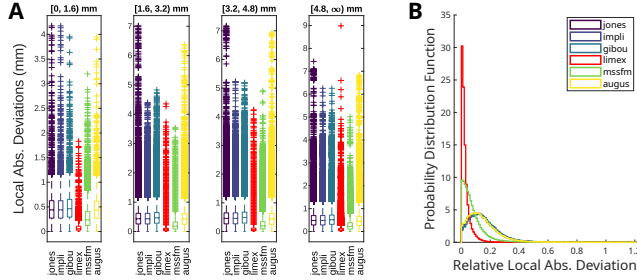#### 4.3.1. Evaluation by Local Thickness

For each of the 757 slices of the RVSC data, the thickness maps were computed using the six methods previously considered: *jones*, *impli*, *gibou*, *limex*, *mssfm* and *augusto*. Here, the processing is performed in 2D to match the dimensionality of the input data and because of the high slice thickness and slice misalignments due to breath hold artifacts. Execution times to obtain the thickness maps with *limex* for the 757 slices, given as median (25th percentile, 75th percentile), were 14.0 s (12.8 s, 15.3 s), which is comparable to the figures of other methods. As with the pig dataset, a silver standard is generated for evaluation purposes for every slice. Each slice is upsampled by a factor of 8 on each of the axes, and the SS thickness map is the average of the six thickness maps obtained with the aforementioned methods on the finest grid. ICC values between the 6 thickness maps computed for the SS were within the interval [0.9231, 0.9997]. Then, the SS thickness values at the vertices of the RV epicardial contour were compared to the values yielded by each of the methods at the original resolution.

(a)

(b)

Figure 10: Boxplot of (a) the L_1 error norms and (b) the L_{∞} error norms of the thickness values at the RV epicardium, of the 757 slices within the RVSC dataset, grouped by the thickness method employed.

Figure 10 contains the boxplots of the L_1 and L_{∞} norms of the 757 slices, grouped by method. It may be observed that the proposed *limex* method obtains the lowest mean L_1 norm (0.115 mm), which was between 55.25% and 76.81% lower than the rest of the methods. *Limex* also achieved the lowest mean L_{∞} norm (0.764 mm), followed by the method *mssfm* (1.292 mm). The behavior of the L_1 norm shown in Fig. 10(a) shows coherence with the results from the pig data and the phantom. A Friedman test was conducted for each of the norms to detect statistical differences between methods, which were found for both norms with $p < 10^{-4}$.

Then, a *post hoc* analysis using the pairwise paired Wilcoxon test with Bonferroni correction for the p-values found statistically significant differences between values of the L_1 norm between every pair of methods. Repeating the *post hoc* analysis for the L_∞ norm, statistically significant differences were found between every pair of methods except between the methods *mssfm* and *augusto*.

Figure 11: A. Boxplots of the local absolute deviations committed by each method on the RVSC dataset, grouped by intervals of the silver standard thickness. B. Probability distribution function of the local relative absolute deviations committed by each method.

To evaluate the behaviour of the different methods with respect to the wall thickness, every vertex of each slice in the RVSC was assigned a group depending on its silver standard thickness value t_n^{ref}. Four intervals were considered, taking into account the acquired in-plane spatial resolution (1.6 mm): $[0, 1.6)$ mm, $[1.6, 3.2)$ mm, $[3.2, 4.8)$ mm and $[4.8, \infty)$ mm. The percentage of vertices that belong to each interval is 2.80%, 43.90%, 38.87% and 14.43%, respectively. Therefore, the percentage of vertices that fall below the acquired in-plane spatial resolution is negligible. Panel A of figure 11 contains the boxplots of the absolute deviations at the vertices of each of the groups. It may be observed that *limex* yields lower errors than the rest of the methods on all intervals. Panel B of figure 11 shows the histograms of the local relative absolute deviations, normalized as probability density functions, of all the compared methods. Local relative absolute deviations were computed as $|t_n - t_n^{\text{ref}}|/t_n^{\text{ref}}$, following the same notation as in Eq. (16), where t_n is calculated for each method.

4.3.2. Evaluation by Myocardial Segments

To evaluate the influence of the thickness method on the detection of myocardial wall thinning or thickening, the following experiment was carried out. For each patient and cardiac phase, the RV was partitioned into myocardial segments according to the model proposed in [37]. End-systole segments were also included to increase the sample size and the number of thick segments. Segments containing less than 5 vertices were removed from the calculations. In total, 1248 segments were considered. For each segment i and thickness method *method*, the segment thickness T_{method}^i was computed by averaging the thickness values at every segment vertex.

Lower and upper thresholds to discriminate in classes thin/normal/thick were established at 3.092 mm and 5 mm, respectively. The lower threshold is the median of the SS thickness values at every point of the epicardium at end-diastole, and the reason for the upper threshold is that it is a marker of disease progression in pulmonary hipertension [36]. Then, each segment i was classified by its value with respect to the SS thickness map as *Thin* if T_{SS}^i was less than 3.092 mm, *Thick* if T_{SS}^i was over 5 mm and *Normal* otherwise. *Thin* and *Thick* segments
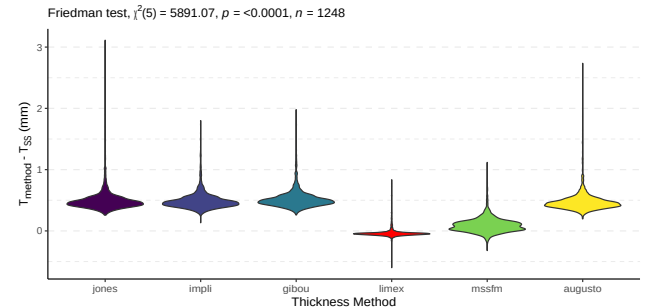
were 37.18% and 8.25% of the total. For each of the methods (*jones*, *impli*, *gibou*, *limex*, *mssfm* and *augusto*), the segments were also classified using the same procedure and the sensitivity ($TP/(TP + FN)$), specificity ($TN/(TN + FP)$) and Dice metrics ($2 \cdot TP/(FP + 2 \cdot TP + FN)$) were computed with respect to the individual *Thin* and *Thick* labels, where TP, TN, FP and FN stand for true positive, true negative, false positive and false negative, respectively. Also, the multi-label accuracy and the multi-label Dice of the *Thin* and *Thick* labels were computed:

$$Multi - label\,Accuracy^{met} = \frac{\sum_{i=1}^{3} C_{ii}^{met}}{\sum_{i=1}^{3} \sum_{j=1}^{3} C_{ij}^{met}} \quad (18)$$

$$Multi - label\,Dice^{met} = 2\frac{C_{11}^{met} + C_{33}^{met}}{\sum_{l=1,3}^{3} \sum_{i=1}^{3} C_{li}^{met} + C_{il}^{met}} \quad (19)$$

where $C \in \mathcal{M}^{3\times3}$ is the confusion matrix such that C_{ij}^{met} is the number of segments labeled i using the silver standard and j using the thickness map provided by method *met* and the label order is {*Thin*, *Normal*, *Thick*}.

Table 1 shows the results attained by each method. *Limex* achieves the best results in all metrics except the specificity of *Thin* segments and the sensitivity of *Thick* segments. Figure 12 shows the violin plot of the values $T_{method}^i - T_{SS}^i$ for each of the methods. The methods *jones*, *impli*, *gibou* and *augusto* present a similar positive bias between 0.475 mm and 0.521 mm, which explains the low classification success of these methods on *Thin* segments. The bias of the *mssfm* is smaller (0.093 mm) and the lowest bias is yielded by *limex* (-0.035 mm). The low bias improves the detection of *Thin* segments, so that the Dice coefficient for *Thin* labels exclusively is 0.924 and 0.973 for *mssfm* and *limex*, respectively. Regarding *Thick* segments, the low bias of *limex* and *mssfm* improves the specificity of the classification, which also leads to higher Dice coefficients with respect to the other methods (0.951 for *limex*). With respect to the multi-label metrics, *limex* was the best method with multi-label accuracy and multi-label Dice values of 0.971 and 0.969, respectively.

Figure 12: Violin plot of the values $T_{method}^i - T_{SS}^i$ generated by each method for the set of myocardial segments.

5. Discussion and Conclusions

A new Locally semi-IMplicit finite difference method with EXtrapolation (*limex*) has been proposed to solve the Laplace equation using the Ghost Fluid philosophy. This method solves the problem

S. Merino-Caviedes, M. Martín-Fernández, M. T. Pérez Rodríguez, M. Á. Martín-Fernández, D. Filgueiras-Rama, F. Simmross-Wattenberg, C. Alberola-López: *Preprint submitted to Elsevier*

Page 11 of 14

Table 1
Results attained by the classification of RV segments of the RVSC dataset using the considered methods.

Method	Thin label only			Thick label only			Multi-label	
	Sensitivity	Specificity	Dice	Sensitivity	Specificity	Dice	Accuracy	Dice
jones	0.437	**1.000**	0.601	**1.000**	0.907	0.658	0.705	0.624
impli	0.437	**1.000**	0.601	**1.000**	0.910	0.667	0.708	0.627
gibou	0.412	**1.000**	0.583	**1.000**	0.900	0.644	0.690	0.603
limex	**0.996**	0.969	**0.973**	0.942	**0.997**	**0.951**	**0.971**	**0.969**
mssfm	0.864	0.996	0.924	0.971	0.985	0.909	0.931	0.921
augusto	0.453	**1.000**	0.623	**1.000**	0.917	0.684	0.720	0.642

of instabilities [15] that arise when the domain boundary is too close to a node location, and the method is grounded on computing the value of nodes contiguous to the boundary as a solution of a linear system of equations posed on the node neighborhood. In addition, these linear systems are used after convergence to provide extrapolated values on the ghost nodes. The computation at contiguous nodes is affordable because the linear systems are posed in such a way that they are updated at each iteration with only a few matrix multiplications. Therefore, the *limex* method is suitable for 3D structures, whereas a fully implicit method requires large amounts of memory. Right ventricular wall thickness is then computed by launching streamlines beginning at the RV epicardium vertices and ending at the endocardium.

Limex has been tested on an analytical phantom, a dataset of segmentations of the 3D biventricular myocardium of pigs and the RVSC dataset, the latter including data from patients with diverse pathologies. In those cases in which a ground truth was not available, a *silver standard* —referred to throughout the paper as SS— has been created as a surrogate. Actually, as pointed out in the literature for 2D ray-tracing-based thickness calculation methods, [33] and [2] explored the relationship between the relative error incurred by the thickness measurements and the relative voxel size and anisotropy. The errors were due to partial volume effects and obliqueness of the tubular structure to the slice plane normal, showing that wall thickness was underestimated with increasing angulation and that this effect increased with voxel anisotropy. Antiga et al. [2] report that, even for a perfectly aligned tubular structure, the measured thickness departs from linearity with the true thickness when the latter is below two pixels wide. This is basically the motivation for the data augmentation stage we have described in Section 3.2.5 as it provides fairness to the experimental results in this respect. Then *limex* has been compared with other thickness computation methods proposed in the literature (*jones*, *mssfm* and *augusto*) and to the streamline method with the solution of the Laplace problem computed with other methods (*impli* and *gibou*). *Limex* has achieved significantly smaller mean values of the L_1 norm than the rest of the methods, and the lowest or second lowest (after the *mssfm*) mean values of the L_∞ norm, in all the considered datasets. Since the *gibou* method also employs ghost nodes to solve the Laplace equation, the improvement in accuracy in *limex* seems due to the extrapolation of the solution to the ghost nodes. Based on our experimental results on coarse anisotropic voxels, for CMR acquisitions with high separation between planes, it would be desirable either to upsample the dataset to isotropic or nearly isotropic resolution for 3D processing or to compute the thickness map using 2D processing. Using such a 2D processing for the RVSC data we have measured the clinical relevance that *limex* provides in terms of classifying segments as thin, normal and thick. This result was implied to some extent in Fig. 11 albeit for

unlocalized points in the myocardium; Table 1 and Fig. 12 provide more conclusive results following a more standard segment-oriented approach. The introduction describes several procedures in which thickness calculation plays an important role in diagnosis and prognosis. The higher classification figures provided by *limex* makes it an interesting candidate for this task.

Also, the different way of defining thickness between *jones* (streamline length) and *augusto* (Euclidean distance between the streamline endpoints) has yielded results statistically different for the L_1 norm. That effect is especially noticeable in the pig data, where the papillary muscles are included in the RV myocardium and, thus, there is a presence of longer streamlines. Therefore, we suggest that the definition of thickness is explicitly stated when reporting thickness values. *Limex* employs the streamline length definition, but it could be easily modified to use the Euclidean distance instead; actually, we have checked that the relative ordering of the methods in terms of L_1 norm coincides with either definition of thickness.

It should be noted that *limex* limits itself to compute the thickness of a given segmentation and does not question its quality. Therefore, considerations about the suitability of different manual (or automatic) segmentation protocols are beyond the scope of this work. Nevertheless, *limex* has outperformed the rest of the methods included in the comparison in the different data sets used for validation, which are rather different from each other: pig data include papillary muscles while the RVSC data do not, and there is presence of several pathologies in the RVSC data. It is important to highlight that the way in which segmentations are provided —label images, countour sets, triangulations or signed distance maps— is relevant, since their intrinsic precision differ; specifically, the precision of label images is limited to the grid resolution while the others have subpixel accuracy. *Limex* profits from this subpixel precision but if the segmentation was given as a label map, the advantage of using it over one of the state of the art methods would not be as noticeable. *Limex*, in addition, needs that at least one pixel/voxel lies within region Ω_R, i.e., within the myocardial wall, so this sets a limitation in the thickness of the structures that our method can tackle as a function of image resolution.

Given that *limex* uses streamlines to compute thickness, it is subject to the pitfalls associated to that class of methods. The method proposed here lessens these problems, but does not completely suppress them. Actually, the results shown in Figs. 10 and 11, together with the robustness to voxel anisotropy shown in Fig. 9 as well as the good behaviour with segment classification shown in Table 1 and Fig. 12, suggest that improvements may be obtained by combining the ideas on which *limex* is grounded with MS-SFM. Specifically, we plan on working on a new scheme for the MS-SFM method that takes advantage of the extrapolation to

the ghost nodes used in *limex* to provide thickness values without the need to explicitly compute streamlines.

6. Acknowledgements

CRediT authorship contribution statement

Susana Merino-Caviedes: Conceptualization, Methodology, Software, Validation, Formal Analysis, Investigation, Visualization, Writing - Original Draft, Writing - Review & Editing. **Marcos Martín-Fernández:** Conceptualization, Formal Analysis, Methodology, Writing - Review & Editing. **María Teresa Pérez Rodríguez:** Conceptualization, Formal Analysis, Methodology, Writing - Review & Editing. **Miguel Ángel Martín-Fernández:** Conceptualization, Formal Analysis, Methodology, Writing - Review & Editing. **David Filgueiras-Rama:** Resources, Data Curation, Formal analysis, Writing - Review & Editing. **Federico Simmross-Wattenberg:** Methodology, Software, Writing - Review & Editing, Funding acquisition. **Carlos Alberola-López:** Conceptualization, Formal Analysis, Methodology, Writing - Review & Editing, Project administration, Funding acquisition.

References

[1] Aitkenhead, A.H., 2013. Mesh voxelisation. URL: https://es.mathworks.com/matlabcentral/fileexchange/27390-mesh-voxelisation. Retrieved on 2020-02-12.

[2] Antiga, L., Wasserman, B., Steinman, D., 2008. On the overestimation of early wall thickening at the carotid bulb by black blood MRI, with implications for coronary and vulnerable plaque imaging. Magn. Reson. Med. 60, 1020–1028. doi:10.1002/mrm.21758.

[3] Astuto, C., Coco, A., Russo, G., 2023. A finite-difference ghost-point multigrid method for multi-scale modelling of sorption kinetics of a surfactant past an oscillating bubble. J. Comput. Phys. 476, 111880. doi:10.1016/j.jcp.2022.111880.

[4] Augusto, J.B., Davies, R.H., Bhuva, A.N., Knott, K.D., Seraphim, A., Alfarih, M., Lau, C., Hughes, R.K., Lopes, L.R., Shiwani, H., Treibel, T.A., Gerber, B.L., Hamilton-Craig, C., Ntusi, N.A.B., Pontone, G., Desai, M.Y., Greenwood, J.P., Swoboda, P.P., Captur, G., Cavalcante, J., Bucciarelli-Ducci, C., Petersen, S.E., Schelbert, E., Manisty, C., Moon, J.C., 2021. Diagnosis and risk stratification in hypertrophic cardiomyopathy using machine learning wall thickness measurement: a comparison with human test-retest performance. Lancet Digit. Health 3, e20–e28. doi:10.1016/S2589-7500(20)30267-3.

[5] Authors/Task Force members, Elliott, P.M., Anastasakis, A., Borger, M.A., Borggrefe, M., Cecchi, F., Charron, P., Hagege, A.A., Lafont, A., Limongelli, G., Mahrholdt, H., McKenna, W.J., Mogensen, J., Nihoyannopoulos, P., Nistri, S., Pieper, P.G., Pieske, B., Rapezzi, C., Rutten, F.H., Tillmanns, C., Watkins, H., Contributor, A., O'Mahony, C., for Practice Guidelines (CPG), E.S.C.C., Zamorano, J.L., Achenbach, S., Baumgartner, H., Bax, J.J., Bueno, H., Dean, V., Deaton, C., Çetin Erol, Fagard, R., Ferrari, R., Hasdai, D., Hoes, A.W., Kirchhof, P., Knuuti, J., Kolh, P., Lancellotti, P., Linhart, A., Nihoyannopoulos, P., Piepoli, M.F., Ponikowski, P., Sirnes, P.A., Tamargo, J.L., Tendera, M., Torbicki, A., Wijns, W., Windecker, S., Reviewers, D., Hasdai, D., Ponikowski, P., Achenbach, S., Alfonso, F., Basso, C., Cardim, N.M., Gimeno, J.R., Heymans, S., Holm, P.J., Keren, A., Kirchhof, P., Kolh, P., Lionis, C., Muneretto, C., Priori, S., Salvador, M.J., Wolpert, C., Zamorano, J.L., Frick, M., Aliyev, F., Komissarova, S., Mairesse, G., Smajić, E., Velchev, V., Antoniades, L., Linhart, A., Bundgaard, H.,

Heliö, T., Leenhardt, A., Katus, H.A., Efthymiadis, G., Sepp, R., Gunnarsson, G.T., Carasso, S., Kerimkulova, A., Kamzola, G., Skouri, H., Eldirsi, G., Kavoliuniene, A., Felice, T., Michels, M., Haugaa, K.H., Lenarczyk, R., Brito, D., Apetrei, E., Bokheria, L., Lovic, D., Hatala, R., Pavía, P.G., Eriksson, M., Noble, S., Srbinovska, E., Özdemir, M., Nesukay, E., Sekhri, N., 2014. 2014 esc guidelines on diagnosis and management of hypertrophic cardiomyopathy: The task force for the diagnosis and management of hypertrophic cardiomyopathy of the european society of cardiology (esc). European Heart Journal 35, 2733–2779. doi:10.1093/eurheartj/ehu284.

[6] Axler, S., Bourdon, P., Ramey, W., 1992. Basic properties of harmonic functions, in: Harmonic Function Theory. Springer New York. volume 137 of *Graduate Texts in Mathematics*, pp. 1–29.

[7] Bae, E., Yuan, J., Tai, X.C., 2011. Global minimization for continuous multiphase partitioning problems using a dual approach. Int. J. Comput. Vis. 92, 112–129. doi:10.1007/s11263-010-0406-y.

[8] Bonnemain, J., Ltaief, Z., Liaudet, L., 2021. The right ventricle in covid-19. J. Clin. Med. 10, 2535. doi:10.3390/jcm10122535.

[9] Coco, A., Mazza, M., Semplice, M., 2023. A ghost-point smoothing strategy for geometric multigrid on curved boundaries. J. Comput. Phys. 478, 111982. doi:10.1016/j.jcp.2023.111982.

[10] Coco, A., Russo, G., 2013. Finite-difference ghost-point multigrid methods on cartesian grids for elliptic problems in arbitrary domains. J. Comput. Phys. 241, 464–501. doi:10.1016/j.jcp.2012.11.047.

[11] Faghihi Langroudi, T., Shabestari, A.A., Hekmati, S., Pourghorban, R., 2021. Association between pulmonary arterial obstruction index and right lateral ventricular wall thickness with in-hospital mortality in patients with acute pulmonary embolism. Emerg. Radiol. 28, 327–331. doi:10.1007/s10140-020-01871-5.

[12] Fedkiw, R.P., Aslam, T., Merriman, B., Osher, S., 1999. A non-oscillatory eulerian approach to interfaces in multimaterial flows (the ghost fluid method). J. Comput .Phys. 152, 457–492. doi:10.1006/JCPH.1999.6236.

[13] Gallinato, O., Poignard, C., 2017. Superconvergent second order Cartesian method for solving free boundary problem for invadopodia formation. J. Comput .Phys. 339, 412–431. doi:10.1016/j.jcp.2017.03.010.

[14] Gibou, F., Fedkiw, R., 2005. A fourth order accurate discretization for the Laplace and heat equations on arbitrary domains, with applications to the Stefan problem. J. Comput. Phys. 202, 577–601. doi:10.1016/j.jcp.2004.07.018.

[15] Gibou, F., Fedkiw, R.P., Cheng, L.T., Kang, M., 2002. A second-order-accurate symmetric discretization of the Poisson equation on irregular domains. J. Comput .Phys. 176, 205–227. doi:10.1006/jcph.2001.6977.

[16] Haberman, R., 1998. Elementary applied partial differential equations : with fourier series and boundary value problems / Richard Haberman. 3rd ed. ed., Prentice-Hall, Englewood Cliffs (New Jersey).

[17] van Hespen, K.M., Zwanenburg, J.J.M., Hendrikse, J., Kuijf, H.J., 2021. Subvoxel vessel wall thickness measurements of the intracranial arteries using a convolutional neural network. Med. Image Anal. 67, 101818. doi:10.1016/j.media.2020.101818.

[18] Jones, S.E., Buchbinder, B.R., Aharon, I., 2000. Three-dimensional mapping of cortical thickness using Laplace's equation. Hum. Brain Mapp. 11, 12–32. doi:10.1002/1097-0193(200009)11:1<12::AID-HBM20>3.0.CO;2-K.

[19] Kwon, O.S., Lee, J., Park, J.W., Yang, S.H., Hwang, I., Yu, H.T., Shin, H., Pak, H.N., 2022. Three-dimensional atrial wall thickness measurement algorithm from a segmented atrial wall using a partial differential equation. IEEE Access 10, 32161–32170. doi:10.1109/ACCESS.2022.3159795.

[20] Li, Q., Pardoe, H., Lichter, R., Werden, E., Raffelt, A., Cumming, T., Brodtmann, A., 2015. Cortical thickness estimation in longitudinal stroke studies: A comparison of 3 measurement methods. Neuroimage Clin. 8, 526–535. doi:10.1016/j.nicl.2014.08.017.

[21] Manning, W.J., Pennell, D. (Eds.), 2019. Cardiovascular Magnetic Resonance: a companion to Braunwald's heart disease. 3rd edition ed., Elsevier, Philadelphia, PA, USA.

[22] McGraw, K.O., Wong, S.P., 1996. Forming inferences about some intraclass correlation coefficients. Psychol. Methods 1, 30–46. doi:10.1037/1082-989X.1.1.30.

[23] Merino-Caviedes, S., Cordero-Grande, L., Perez, M.T., Casaseca-de-la Higuera, P., Martin-Fernandez, M., Deriche, R., Alberola-Lopez, C., 2019. A second order multi-stencil Fast Marching method with a non-constant local cost model. IEEE Trans. Image Process. 28, 1967–1979.

[24] Merino-Caviedes, S., Cordero-Grande, L., Revilla-Orodea, A., Sevilla-Ruiz, T., Perez, M.T., Martin-Fernandez, M., Alberola-Lopez, C., 2014. Multi-stencil streamline fast marching: a general 3-d framework to determine myocardial thickness and transmurality in late enhancement images. IEEE Trans. Med. Imaging 33, 23–37. doi:10.1109/TMI.2013.2276765.

[25] Merino-Caviedes, S., Gutierrez, L.K., Alfonso-Almazán, J.M., Sanz-Estébanez, S., Cordero-Grande, L., Quintanilla, J.G., Sánchez-González, J., Marina-Breysse, M., Galán-Arriola, C., Enríquez-Vázquez, D., Torres, C., Pizarro, G., Ibáñez, B., Peinado, R., Merino, J.L., Pérez-Villacastín, J., Jalife, J., López-Yunta, M., Vázquez, M., Aguado-Sierra, J., González-Ferrer, J.J., Pérez-Castellano, N., Martín-Fernández, M., Alberola-López, C., Filgueiras-Rama, D., 2021. Time-efficient three-dimensional transmural scar assessment provides relevant substrate characterization for ventricular tachycardia features and long-term recurrences in ischemic cardiomyopathy. Sci. Rep. 11, 18722. doi:10.1038/s41598-021-97399-w.

[26] Nazarian, S., Bluemke, D.A., Lardo, A.C., Zviman, M.M., Watkins, S.P., Dickfeld, T.L., Meininger, G.R., Roguin, A., Calkins, H., Tomaselli, G.F., Weiss, R.G., Berger, R.D., Lima, J.A.C., Halperin, H.R., 2005. Magnetic resonance assessment of the substrate for inducible ventricular tachycardia in nonischemic cardiomyopathy. Circulation 112, 2821–2825. doi:10.1161/CIRCULATIONAHA.105.549659.

[27] Peng, P., Lekadir, K., Gooya, A., Shao, L., Petersen, S.E., Frangi, A.F., 2016. A review of heart chamber segmentation for structural and functional analysis using cardiac magnetic resonance imaging. Magn. Reson. Mater. Phys. Biol. Med. 29, 155–195. doi:10.1007/s10334-015-0521-4.

[28] Perazzolo Marra, M., Leoni, L., Bauce, B., Corbetti, F., Zorzi, A., Migliore, F., Silvano, M., Rigato, I., Tona, F., Tarantini, G., Cacciavillani, L., Basso, C., Buja, G., Thiene, G., Iliceto, S., Corrado, D., 2012. Imaging study of ventricular scar in arrhythmogenic right ventricular cardiomyopathy. Circulation: Arrhythmia and Electrophysiology 5, 91–100. doi:10.1161/CIRCEP.111.964635.

[29] Petitjean, C., Zuluaga, M., Bai, W., Dacher, J., Grosgeorge, D., Caudron, J., Ruan, S., Ben Ayed, I., Cardoso, M., H.C., C., Jimenez-Carretero, D., Ledesma-Carbayo, M., Davatzikos, C., Doshi, J., Erus, G., Maier, O., C.M.S., N., Ou, Y., Ourselin, S., Peng, C., Peters, N., Peters, T., Rajchl, M., Rueckert, D., Santos, A., Shi, W., Wang, C., Wang, H., Yuan, J., 2015. Right ventricle segmentation from cardiac MRI: A collation study. Med. Image Anal. 19, 187–202. doi:10.1016/j.media.2014.10.004.

[30] Prasad, M.N., Brown, M.S., Ni, C., Margolis, D., Douek, M., Raman, S., Lu, D., Goldin, J.G., Warfield, S.K., 2009. Reproducibility of laplacian wall thickness measurements of the gallbladder with varying ct slice thickness. J. Signal Process. Syst. 55, 67–75. doi:10.1007/s11265-008-0199-1.

[31] Salerno, M., Sharif, B., Arheden, H., Kumar, A., Axel, L., Li, D., Neubauer, S., 2017. Recent Advances in Cardiovascular Magnetic Resonance. Circ. Cardiovasc. Imaging 10. doi:10.1161/CIRCIMAGING.116.003951.

[32] Sano, H., Tanaka, H., Motoji, Y., Fukuda, Y., Mochizuki, Y., Hatani, Y., Matsuzoe, H., Hatazawa, K., Shimoura, H., Ooka, J., Ryo-Koriyama, K., Nakayama, K., Matsumoto, K., Emoto, N., Hirata, K., 2017. Right ventricular relative wall thickness as a predictor of outcomes and of right ventricular reverse remodeling for patients with pulmonary hypertension. Int. J. Cardiovasc. Imaging 33, 313–321. doi:10.1007/s10554-016-1004-z.

[33] Sato, Y., Tanaka, H., Nishii, T., Nakanishi, K., Sugano, N., Kubota, T., Nakamura, H., Yoshikawa, H., Ochi, T., Tamura, S., 2003. Limits on the accuracy of 3-d thickness measurement in magnetic resonance images- effects of voxel anisotropy. IEEE Trans. Med. Imaging 22, 1076–1088. doi:10.1109/TMI.2003.816955.

[34] Schuijf, J.D., Kaandorp, T.A.M., Lamb, H.J., van der Geest, R.J., Viergever, E.P., van der Wall, E.E., de Roos, A., Bax, J.J., 2004. Quantification of myocardial infarct size and transmurality by contrast-enhanced magnetic resonance imaging in men. Am. J. Cardiol. 94, 284–288. doi:10.1016/j.amjcard.2004.04.020.

[35] Scudiero, F., Silverio, A., Muraca, I., Russo, V., Di Maio, M., Silvestro, A., Personeni, D., Citro, R., Canonico, M.E., Galasso, G., Porto, I., Parodi, G., 2022. Long-Term Prognostic Impact of Right Ventricular Dysfunction in Patients with COVID-19. J. Pers. Med. 12, 162. doi:10.3390/jpm12020162.

[36] Seo, H.S., Lee, H., 2018. Assessment of right ventricular function in pulmonary hypertension with multimodality imaging. Journal of Cardiovascular Imaging 26, 189. doi:10.4250/jcvi.2018.26.e28.

[37] Tokodi, M., Staub, L., Budai, Á., Lakatos, B.K., Csákvári, M., Suhai, F.I., Szabó, L., Fábián, A., Vágó, H., Tősér, Z., Merkely, B., Kovács, A., 2021. Partitioning the right ventricle into 15 segments and decomposing its motion using 3d echocardiography-based models: The updated revision method. Frontiers in Cardiovascular Medicine 8, 622118. URL: https://www.frontiersin.org/articles/10.3389/fcvm.2021.622118/full, doi:10.3389/fcvm.2021.622118.

[38] Wang, Y., Xiong, Z., Nalar, A., Hansen, B.J., Kharche, S., Seemann, G., Loewe, A., Fedorov, V.V., Zhao, J., 2019. A robust computational framework for estimating 3d bi-atrial chamber wall thickness. Computers in Biology and Medicine 114. doi:10.1016/J.COMPBIOMED.2019.103444.

[39] Yezzi, A.J., Prince, J.L., 2003. An eulerian pde approach for computing tissue thickness. IEEE Trans. Med. Imaging 22, 1332–1339. doi:10.1109/TMI.2003.817775.

[40] Zhuang, X., 2013. Challenges and methodologies of fully automatic whole heart segmentation: A review. J. Healthc. Eng. 4, 371–408. doi:10.1260/2040-2295.4.3.371.